Geophysical Research Letters

RESEARCH LETTER
10.1029/2023GL104402

Upper Mantle Anisotropy and Flow Beneath the Pacific Ocean Revealed by Differential PS-SKS Splitting

Jonathan Wolf[1] and **Maureen D. Long**[1]

[1]Department of Earth and Planetary Sciences, Yale University, New Haven, CT, USA

Key Points:

- We test the robustness of differential PS-SKS shear-wave splitting measurements to characterize anisotropy near the PS bounce point
- We use this technique infer seismic anisotropy beneath the Pacific Ocean
- A majority of our measurements can be explained by plate motion induced shearing beneath the Pacific plate

Correspondence to:

J. Wolf,
jonathan.wolf@yale.edu

Citation:

Wolf, J., & Long, M. D. (2023). Upper mantle anisotropy and flow beneath the Pacific Ocean revealed by differential PS-SKS splitting. *Geophysical Research Letters*, *50*, e2023GL104402. https://doi.org/10.1029/2023GL104402

Received 3 MAY 2023
Accepted 10 AUG 2023

Author Contributions:

Conceptualization: Jonathan Wolf, Maureen D. Long
Formal analysis: Jonathan Wolf
Funding acquisition: Maureen D. Long
Investigation: Jonathan Wolf
Methodology: Jonathan Wolf, Maureen D. Long
Resources: Maureen D. Long
Software: Jonathan Wolf
Supervision: Maureen D. Long
Validation: Jonathan Wolf
Visualization: Jonathan Wolf
Writing – original draft: Jonathan Wolf
Writing – review & editing: Jonathan Wolf, Maureen D. Long

Abstract Upper mantle anisotropy has been mapped beneath continents at high spatial resolution. Beneath the oceans, however, shear wave splitting constraints on upper mantle anisotropy are sparse, due to the paucity of seismic receivers. A technique that does not require the availability of seismic stations close to the region under study is differential PS-SKS splitting. Here, we use global wavefield simulations to investigate circumstances under which PS-SKS splitting can be applied, and then use this technique to measure upper mantle anisotropy beneath the Pacific Ocean basin. Our results demonstrate that upper mantle anisotropy in our study region mostly reflects shearing due to the Pacific plate. North of Fiji, we observe a rotation of fast polarization directions, away from the direction of absolute plate motion of the Pacific plate. This may reflect far-field mantle flow effects associated with the subduction of the Australian plate beneath the Pacific.

Plain Language Summary Earthquakes cause seismic waves whose speeds sometimes depend on their polarization and propagation direction. This material property, called seismic anisotropy, can be used to infer the direction of flow in Earth's upper mantle. Seismic anisotropy is straightforward to measure directly beneath a seismic station, but harder to study if station coverage is sparse. We use a technique that allows us to infer upper mantle seismic anisotropy beneath the Pacific Ocean in places without nearby seismic stations. Our measurements show that while seismic anisotropy varies laterally beneath the Pacific Ocean, in most cases it can be explained by the movement of the Pacific tectonic plate, leading to horizontal shearing of the underlying mantle. North of Fiji, we can observe the effects that the subduction of the Australian beneath the Pacific tectonic plate has on upper mantle flow.

1. Introduction

Seismic anisotropy, or the dependence of seismic wavespeeds on polarization or propagation direction of the wave, has been extensively studied in the upper mantle (e.g., Liu et al., 2014; Savage, 1999; Silver, 1996; Zhu et al., 2020). It can be characterized using surface waves, which permit a relatively good depth resolution of seismic anisotropy (e.g., Panning & Nolet, 2008; Yu & Park, 1993; Yuan & Beghein, 2014); alternatively, shear-wave splitting of body waves can be used for a higher lateral resolution (e.g., Lopes et al., 2020; Russo et al., 2010; Walpole et al., 2014). The typical motivation to study seismic anisotropy is to map mantle deformation and flow (e.g., Karato et al., 2008). The fast polarization direction of upper mantle anisotropy often aligns with plate motions (e.g., Becker & Lebedev, 2021; Long & Becker, 2010; Silver, 1996), although there are some exceptions, particularly in subduction zones (e.g., Kneller et al., 2005; Long, 2013). Therefore, measurements of upper mantle seismic anisotropy are a powerful tool to map the global upper mantle flow field.

Measurements of shear-wave splitting are commonly applied to SKS, SKKS, and PKS (*KS) phases and are generally thought to mainly reflect seismic anisotropy in the upper mantle beneath the station (e.g., Liu et al., 2014; Silver, 1996; Walpole et al., 2014), although contributions from the lowermost mantle are possible (e.g., Grund & Ritter, 2018; Lynner & Long, 2012; Niu & Perez, 2004; Wolf & Long, 2022; Wolf et al., 2019). *KS are popular target phases because they are initially radially polarized due to the P to SV conversion at the core-mantle boundary (CMB). Splitting measurements from *KS phases have been applied to a large number of stations across the globe, and many measurements have been made available in open access databases (e.g., Barruol et al., 2009; Liu et al., 2014; Trabant et al., 2012). These databases give an excellent overview of upper mantle splitting world-wide, although there are some poorly sampled areas. The abundance of splitting data is controlled by the station density in any particular region. For example, data coverage is sparse beneath ocean basins (e.g., Barruol et al., 2009; Liu et al., 2014; Trabant et al., 2012) because seismic receivers are difficult and expensive to install there.

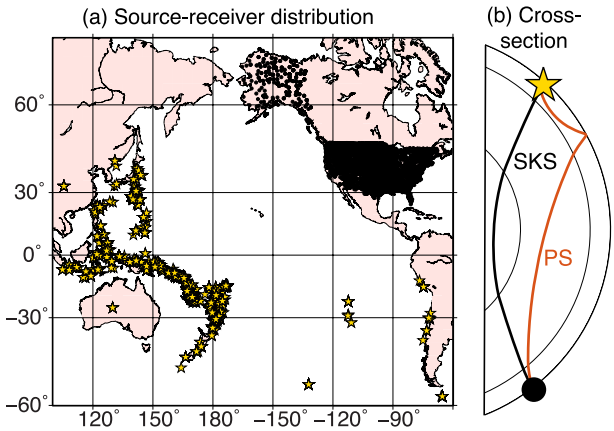

Figure 1. (a) Source-receiver distribution for all event-station pairs for which at least one well-constrained differential PS-SKS splitting intensity measurement could be obtained. Events are represented as yellow stars and stations as black circles. (b) Cross-section showing SKS (black) and PS (red) raypaths for an epicentral distance of 110°.

Su and Park (1994) suggested that the global resolution of upper mantle anisotropy can be improved by comparing shear-wave splitting of PS and SKS phases (Figure 1b), a method that has not been used since. PS and SKS are both initially SV polarized before sampling anisotropy due to the P-SV conversions along their raypaths. They both sample similar upper mantle anisotropy beneath the receiver; however, PS additionally accumulates splitting on the portion of its raypath that travels through upper mantle anisotropy after bouncing off the surface. Therefore, differential splitting of PS and SKS for the same station-event pair, or for sets of waves with similar paths, indicates an upper mantle anisotropy contribution close to the PS bounce point. If seismic stations are available in the vicinity of the PS bounce point, there is no clear advantage of using PS-SKS splitting instead of traditional SKS splitting measurements. However, if no seismic stations are available, then PS-SKS splitting is an excellent option. Thus, PS-SKS splitting holds potential to fill in sampling gaps of upper mantle anisotropy studies, particularly beneath ocean basins.

In this study, we analyze upper mantle anisotropy beneath the Pacific Ocean, which has only been sparsely sampled to date using shear wave splitting measurements (e.g., Barruol et al., 2009; Liu et al., 2014; Trabant et al., 2012). We apply the PS-SKS splitting technique to events with moment magnitudes >6.0 that occurred between January 2006 and December 2022 in an epicentral distance of 90°–115° from USArray (IRIS Transportable Array, 2003) stations, in the continental United States and Alaska. This allows us to construct a large data set (consisting of 320,000 seismograms in total; Figure 1a). We show that fast polarization directions of upper mantle anisotropy tend to align with the absolute plate motion of the Pacific plate for much of our study region; however, far-field effects on flow from the circum-Pacific subduction zones complicate this pattern.

2. Shear-Wave Splitting Measurements

When a shear wave travels through an anisotropic medium, it splits into two components, one traveling relatively slow and the other traveling fast. The time delay between these two components is usually referred to as δt, while the polarization direction of the fast traveling wave (measured clockwise from the north) is called ϕ. We call the fast polarization direction measured at the station ϕ_R. This parameter, translated to the bounce point reference frame for PS, can be expressed via $\phi = b - (\phi_R - b)$, with b denoting the backazimuth. This conversion to the bounce point geographical frame is necessary because the PS wave accumulates splitting close to the bounce point on the downgoing (but not upgoing) raypath leg. Therefore, the fast polarization direction needs to be reflected across the backazimuthal direction, analogous to the conversion commonly applied for source-side S splitting measurements (e.g., Lynner & Long, 2014; Russo et al., 2010).

A parameter that can be used to define the strength of splitting for a given seismogram is the splitting intensity (Chevrot, 2000), SI, defined as

$$SI = -2\frac{T(t)R'(t)}{|R'(t)|^2} \approx \delta t \sin[2(b - \phi_R)] \quad (1)$$

where $R(t)$ is the radial component, $R'(t)$ is the time derivative of the radial component and $T(t)$ is the transverse component. The splitting intensity is large if the transverse component, $T(t)$, and the radial component time derivative, $R'(t)$, have a similar waveform shape, and if the amplitude of the transverse component is large, reflecting energy that has been partitioned from the radial to the transverse component. The 95% confidence interval of SI is determined using the formulas from the appendix of Chevrot (2000).

We use SplitRacer_auto (Link et al., 2022; Reiss & Rümpker, 2017) to automatically measure the splitting parameters (ϕ, δt, and SI) for our large PS-SKS data set. We filter our data retaining periods between 6 and 25 s. Then, we calculate splitting parameters for 30 randomly selected time windows, and only retain measurements if they are largely independent of the measurement window. SplitRacer_auto uses the transverse component

minimization technique (Silver & Chan, 1991), and calculates 95% confidence intervals using the corrected algorithm of Walsh et al. (2013). We modify SplitRacer_auto slightly to be able to make splitting measurements for PS phases.

3. PS-SKS Splitting: Method Verification

At an epicentral distance of ~90°, SKS starts to be clearly separated from S and ScS. The PS turning point in the mantle is more than 500 km above the CMB for epicentral distances <115°, such that no major contribution from deep mantle anisotropy (typically confined to D′′ layer; e.g., Panning & Romanowicz, 2006) is expected to influence PS at these distances. We therefore choose to investigate PS-SKS splitting in the epicentral distance range between 90° and 115°.

Before we can apply the PS-SKS splitting technique systematically, however, we explore two possible sources of uncertainty. First, while the raypaths of PS and SKS are similar in the upper mantle beneath the receiver, they are not completely identical (Figure 1b). We therefore investigate the threshold difference in PS and SKS splitting for which differential splitting is robustly indicative of anisotropy close to the PS bounce point. Second, we investigate whether SP, which arrives at the same time as PS for a focal depth of 0 km but mainly on the vertical component, does influence the measured PS splitting parameters. To explore these two questions we use global wavefield simulations with AxiSEM3D (Leng et al., 2016, 2019), following previous work (Tesoniero et al., 2020; Wolf & Long, 2023; Wolf et al., 2022b, 2023).

For our simulations we always place the source at the North Pole, simulating an earthquake with either 0 or 500 km focal depth. The background velocity structure in our simulations is always isotropic PREM (Dziewonski & Anderson, 1981), which is replaced at certain depths in the upper mantle by seismic anisotropy. To describe the seismic anisotropy, we use the olivine elastic tensors from Table 21.1 in Karato (2008) for the fabric types that are potentially widespread in the upper mantle (A, C, and E), assuming a horizontal simple shear configuration. These fabric types occur under different temperature, stress, and different water contents and have different elastic properties. We incorporate these elastic tensors starting at a depth of 24 km and then adjust the anisotropic layer thickness such that the maximum (sampling azimuth dependent) delay time (depending on the sampling azimuth) is ~1 s. The starting depth is selected arbitrarily, and the maximum delay time is selected to represent moderate splitting.

In the first set of simulations we investigate the maximum difference in PS and SKS splitting for an anisotropic layer beneath the receiver and no seismic anisotropy at the bounce point. To test this, we conduct simulations for an epicentral distance of 90° (Figure 2a inset), for which the spatial separation of PS and SKS raypaths in the upper mantle beneath the receiver is the largest. We simulate an earthquake at 500 km depth, whose focal mechanism is chosen to maximize PS and SKS amplitudes by yielding an initially fully radially polarized S wave, with M_{tt} as the only non-zero component of the moment tensor (corresponding to a strike direction of 0°). The event initial polarization is chosen to lead to high-amplitude SKS arrivals but is arbitrary apart from this. Our results in these simulations mainly depend on the difference of PS and SKS raypaths in the receiver side upper mantle and are therefore largely independent of source depth. We rotate the A-, C-, and E-type elastic tensors around the vertical axis in increments of 15°, thus sampling different portions of the tensor with propagating PS and SKS waves, and measure PS and SKS splitting intensities (Figures 2a–2c).

We find that while the detailed patterns depend on the fabric type, upper mantle anisotropy beneath the receiver leads to *SI* differences up to 0.4 s between PS and SKS (Figures 2a–2c). Splitting intensity differences of PS and SKS phases depend on the olivine fabric type and the orientation of the anisotropy (Figures 2a–2c). For example, *SI* difference patterns vary for a fast axis dip angle of 45°, although the absolute value is always <0.4 s irrespective of the rotation angle (Figures 2a–2c). As described above, we test moderate strengths of upper mantle splitting. For weaker splitting close to the receiver, the 0.4 s *SI* difference threshold will likely be lower and for stronger splitting, higher. However, such effects at single stations can be mitigated either by binning and stacking data from multiple events, or by focusing on source-event pairs for which the upper mantle beneath the receiver leads to null SKS splitting. We will use both approaches in our analysis.

To test whether the contemporaneous SP arrival influences the measured PS splitting parameters, we conduct a second set of simulations. We simulate a strike-slip and a normal faulting event with a focal depth of 0 km and a strike direction of 0° at the North Pole and place stations at an epicentral distance of 100°, spaced every 5° in longitude (Figures 2d and 2e inset). We measure PS-SKS splitting for waves arriving from backazimuths from 0° to 90°. This measures energy from one quadrant of the moment tensor, thereby effectively varying PS/SP

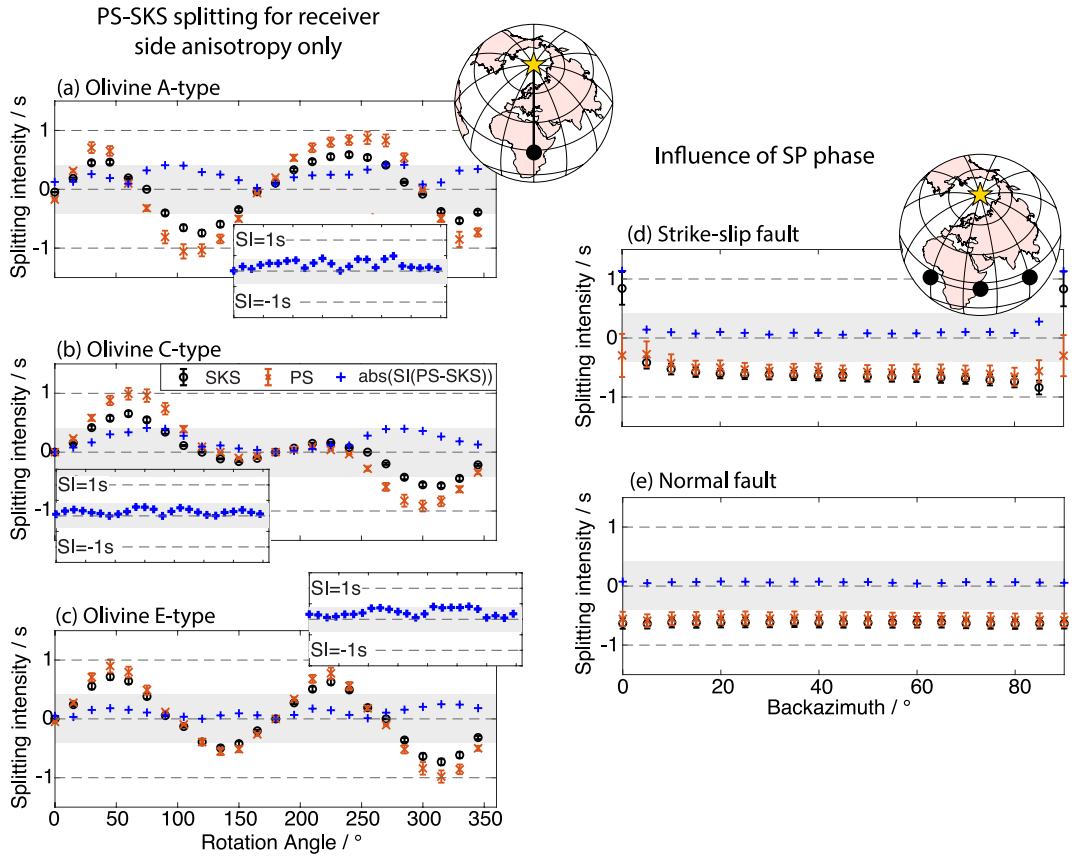

Figure 2. Results from global wavefield simulations that investigate (a–c) PS-SKS splitting in the presence of (only) receiver side anisotropy and (d, e) the influence of the SP phase on splitting parameters. (a) PS (red) and SKS (black) splitting intensities along with their absolute differences (blue) as a function of rotation angle (in the horizontal plane) of an olivine A-type elastic tensor (see text) in a horizontal simple shear configuration. Gray shading indicates splitting intensities between −0.4 s and 0.4 s. The source-receiver configuration is shown on the inset at top right. The inset at the bottom shows the *SI* difference results from analogous simulations for a fast axis with a dip angle of 45°. (b) Same as (a) for an olivine C-type elastic tensor. (c) Same as (a) for an olivine E-type elastic tensor. (d) PS (red) and SKS (black) splitting intensities and their absolute differences (blue) as a function of backazimuth for an olivine A-type elastic tensor and a strike-slip event. Other plotting conventions are as in panel (a). (e) Same as panel (d) for a normal fault event.

amplitudes as a function of backazimuth. For all simulations, we incorporate the same olivine A-type elastic tensor in the upper mantle, such that splitting parameters should be independent of backazimuth. For the strike-slip event, for backazimuths around 0° and 90°, there is little initial SV energy due to the radiation pattern; in practice, such seismograms would be discarded in the pre-processing (Figure 2d). Apart from that, for both the strike-slip (Figure 2d) and the normal fault event (Figure 2e), PS splitting intensities are essentially the same regardless of backazimuth. Thus, we infer that the influence of different PS-SP amplitudes on PS splitting measurements is negligible, and SP cannot be expected to interfere substantially with PS splitting measurements.

Summarizing our modeling results, we have shown that PS-SKS splitting intensity differences greater than ∼0.4 s can likely be attributed to anisotropy near the PS bounce point. This 0.4 s cutoff is chosen considering a worst-case scenario with an epicentral distance of 90° (Figures 2a–2c). Additionally, we have demonstrated that SP does not interfere strongly with PS splitting, which enables us to measure PS-SKS splitting for any focal depth (Figures 2d and 2e).

4. Results

From our USArray data set, we obtain ∼6,000 PS-SKS pairs for which both phases have well-constrained splitting intensities, which we define as having a maximum size of the 95% confidence interval of ±0.4 s. We additionally obtain 30 splitting measurements for which SKS splitting is null ($|SI| < 0.3$ s) and ϕ-δt-measurements for

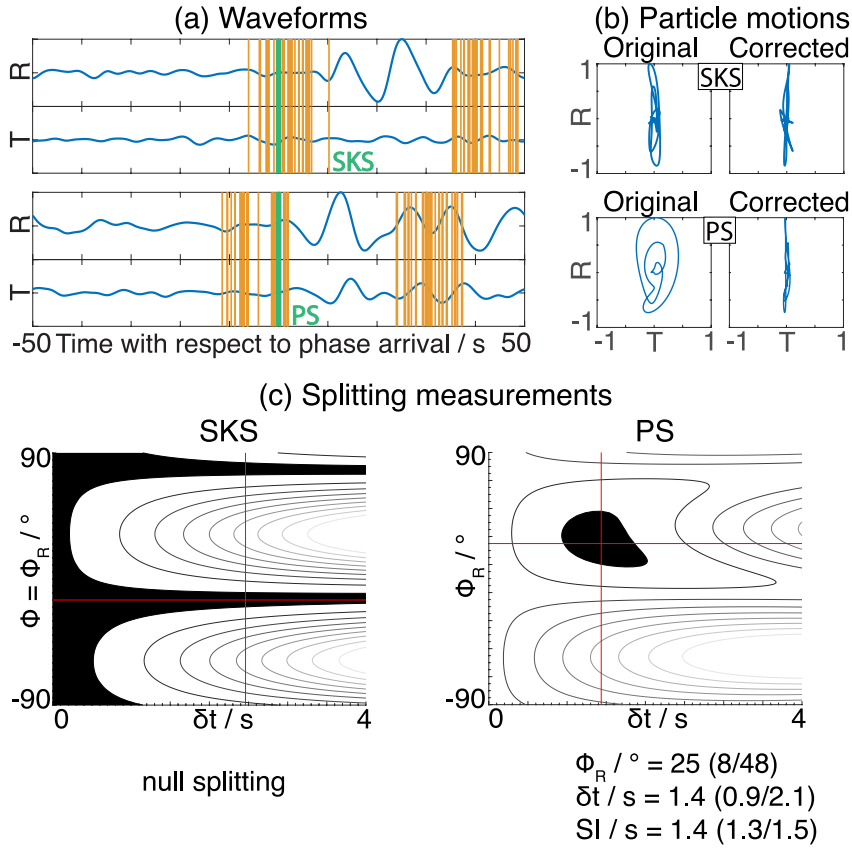

Figure 3. Differential PS-SKS splitting measured at station Q31A for an event that occurred on 11 August 2010 (moment magnitude: 7.3; focal depth: 34 km; distance: 103°; and backazimuth: 258°). (a) SKS (top) and PS (bottom) radial (R) and transverse (T) waveforms. The PREM-predicted phase arrival time is shown by a light green line and the start/end of the automatically selected measurement windows are shown as orange lines. SKS transverse energy is at the noise amplitude level; therefore, SKS splitting is null. (b) PS particle motions before (left) and after (right) correcting for the phase's best fitting splitting parameters. Both are linear for SKS whose splitting is null (top), while only the corrected particle motion of the split PS phase is linear (bottom). (c) Best fitting splitting parameters (crossing red lines) for SKS (left) and PS (right) in the ϕ_R-δt plane. The 95% confidence interval is shown in black. SKS splitting is null, while ϕ, δt, and *SI*, given by the values at lower right, are well-constrained for PS.

PS are well-constrained. We consider PS (ϕ, δt) measurements well-constrained whenever the size of the 95% confidence intervals is smaller than ±25° for ϕ and ±1.0 s for δt. A splitting measurement example for such a PS-SKS pair is shown in Figure 3. In this case, the SKS transverse component energy is close to the noise level, suggesting null or near-null splitting; in contrast, we can observe clear PS splitting. Since SKS splitting is null, PS splitting can mainly be attributed to bounce point anisotropy. Besides the splitting intensity, for this example ϕ and δt are also well-constrained for PS, revealing the fast polarization direction and time delay associated with upper mantle anisotropy near the bounce point.

To increase the number of useable measurements, we also implement an alternative approach that does not only focus on PS-SKS pairs for the same source and receiver. For every well-constrained PS splitting intensity measurement, we calculate the average SKS splitting intensity at the station in a 5° backazimuthal swath around the incoming PS backazimuth. We then calculate the *SI* difference between the PS measurement and the SKS average for the bin. In a similar way, we backazimuthally bin SKS to obtain reliable (ϕ, δt) measurements for PS: If at least 70% of the SKS *SI* measurements in a backazimuthal bin of up to 10° around the PS backazimuth are null, we report well-constrained (ϕ, δt) measurements from PS. If we can obtain a sufficient number (~10) of well-constrained SKS measurements in a tighter bin than 10° around the backazimuthal direction of whom 70% are null (avoiding potential backazimuthal spread of values), we also report the PS splitting measurement. Using this approach, we increase the number of useable *SI* and (ϕ, δt) measurements between two- to three-fold, thereby increasing coverage. Importantly, the general patterns are the same as when we use PS-SKS pairs (Figure 4).

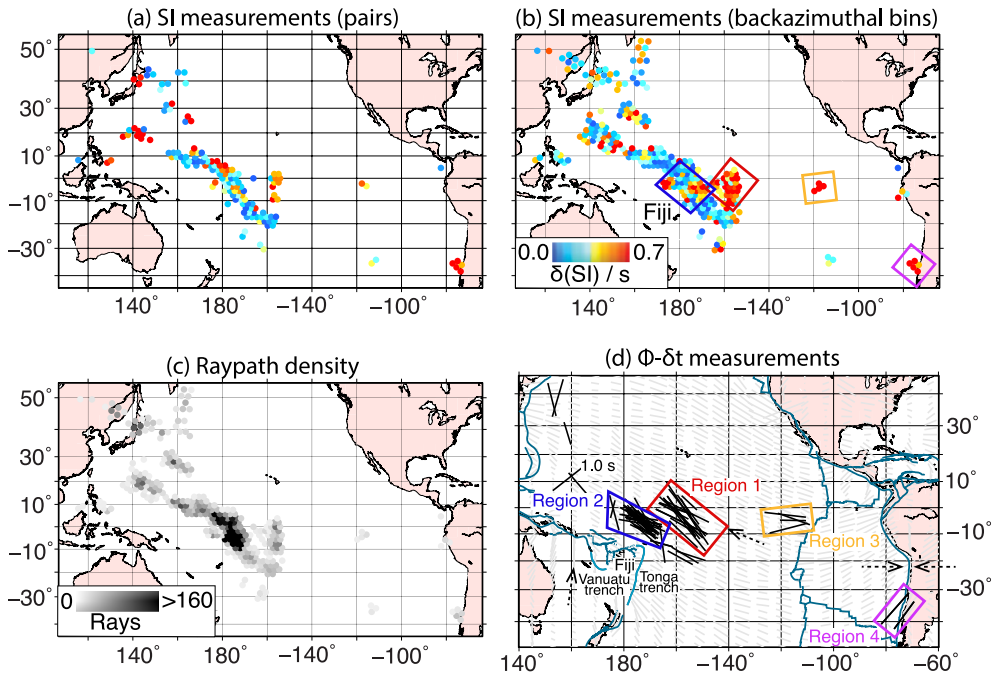

Figure 4. Differential PS-SKS splitting results. (a) Average PS-SKS splitting intensity discrepancies plotted at the PS bounce point and binned spatially (δSI, see legend) for a bin size of 2.5° × 2.5° only using PS-SKS pairs from the same seismogram. (b) Same as panel (a) using the backazimuthal averaging of SKS splitting parameters described in Section 4. Distinct regions (1–4) with high splitting intensity discrepancies are marked as colored boxes. (c) Number of measurements per bin (see legend) for the differential *SI* measurements shown in panel (b). (d) Well-constrained PS (ϕ, δt) measurements (black sticks) for null SKS splitting, plotted in ray-centered coordinates at the PS bounce point, using backazimuthal averaging of splitting parameters. The same four regions are marked as in panel (b). Dashed arrows represent absolute plate motions (DeMets et al., 2010). Plate boundaries (Coffin et al., 1997) are shown by blue lines. Light gray lines indicate azimuthal anisotropy at 200 km depth from Debayle et al. (2016).

In general, splitting intensity discrepancies will depend on the sampling direction of the anisotropy, as well as on the strength and geometry of anisotropy. However, since all data sample the upper mantle from a similar direction in any particular region in our data set, it is useful to average our differential splitting intensity measurements in spatial bins, since individual data points (plotted at the PS bounce point) lie on top of each other (Figures 4a and 4b). We bin our bounce point splitting data using bins with a size of 2.5° × 2.5°; the results are shown in Figures 4a and 4b. We select this bin size as the approximate radius of the first Fresnel zone for PS, assuming a dominant period of 10 s and a source-receiver distance of 110°, inferred following Su and Park (1994). (Strictly speaking, the shape of the first Fresnel zone will be elliptical, but we neglect this for the purpose of this calculation.)

We first focus on spatial patterns of differential PS-SKS splitting intensity discrepancies. We can identify four distinct anisotropic regions labeled 1–4 in Figure 4b. For the identification of these regions we only focus on clusters of bins that indicate strong PS-SKS splitting discrepancies (Figure 4b), and only select those bins that exhibit a good ray coverage (Figure 4c) with more than 10 measurements per bin. The distribution of those regions illustrates that the upper mantle beneath the Pacific Ocean is anisotropic in many areas. We emphasize that with our approach, we are not able to exclude the possibility of upper mantle anisotropy in regions that do not exhibit large PS-SKS splitting discrepancies. While the absence of seismic anisotropy is one explanation for low PS-SKS splitting intensity discrepancies, another explanation is that the upper mantle seismic anisotropy close to the PS bounce point is sampled from a direction that does not lead to strong PS splitting (i.e., a null direction).

More informative than the differential PS-SKS splitting intensities are measurements of fast polarization directions and delay times caused by upper mantle anisotropy close to the PS bounce point. To avoid applying explicit ray-theoretical corrections for receiver side upper mantle anisotropy, which can have significant uncertainties (Wolf et al., 2022a), we focus on PS measurements for which (ϕ, δt) is well-constrained and the corresponding SKS splitting is null, using either the PS-SKS pair approach or the SKS backazimuthal binning approach. For

the anisotropic regions marked in Figure 4b, we obtain multiple well-constrained (ϕ-δt) measurements for PS (Figure 4d). Fast polarization directions are oriented roughly east-southeast/west-northwest for regions 1 and 2 (Figure 4d); average delay times are approximately 30% larger for region 2. In the west of region 2, fast polarization directions are oriented almost south/north. Region 3 shows approximately east/west fast directions, and region 4 southwest/northeast fast direction orientations. Most of the other measurements are scattered across different locations and generally show no consistent orientation of fast polarization directions.

5. Discussion

For much of our study region, no traditional SKS splitting measurements are available in global databases. Measurements made using ocean bottom seismometer (Takeo et al., 2016) data and using ocean island stations (Fontaine et al., 2007) around French Polynesia, to the south and east of regions 1 and 2 (Figure 4d), show fast polarization directions that generally align with the absolute plate motion direction of the Pacific plate. Previous PS-SKS splitting results from Su and Park (1994) focused on a region slightly to the south of region 2, and agree with the fast polarization directions measured in this study. Additionally, patterns of azimuthal anisotropy at ~200 km depth that have been inferred from surface waves in multiple studies (e.g., Becker, 2012; Debayle et al., 2016; Eddy et al., 2022; Lebedev & Van Der Hilst, 2008; Yuan & Beghein, 2014) are similar to our measurements in regions 1 and 2 (Figure 4d). Taken together, our results and the results from previous studies suggest consistent east-southeast oriented fast directions in and around regions 1 and 2. These fast polarization directions agree well with the direction of absolute plate motion of the Pacific plate (Figure 4d), and are therefore likely primarily caused by plate motion induced shearing in the asthenospheric upper mantle.

In the west of region 2, we can observe a rotation of fast polarization directions to being nearly south-north (Figure 4d). However, given the limited number of measurements, it is unclear how robust this trend is. This geometry is generally consistent with some azimuthal anisotropy models derived from surface waves (e.g., Eddy et al., 2022; Yuan & Beghein, 2014), which show weak anisotropy in this region for depths >100 km and approximately north-northeast fast polarization directions above that depth. In fact, measurements of azimuthal anisotropy from surface waves show fast polarization directions that differ from the direction of absolute plate motion in regions adjacent ot circum-Pacific subduction zones (e.g., Debayle et al., 2016; Eddy et al., 2022; Yuan & Beghein, 2014). We hypothesize that the rotation of fast polarization directions in the west of region 2 may be caused by far-field effects of three dimensional flow associated with the subduction of the Australian underneath the Pacific plate (Faccenda & Capitanio, 2012; Paczkowski et al., 2014).

Measurements in region 3 agree well with surface wave models (e.g., Debayle et al., 2016; Eddy et al., 2022; Yuan & Beghein, 2014) and with the direction of absolute plate motion. We also compare our measured fast polarization directions in region 4 to surface-wave derived azimuthal anisotropy, and find they agree well. Additionally, region 4 fast directions agree well with previous SKS splitting results from Hicks et al. (2012) just to the north. This direction is not parallel to the absolute motion of the Nazca plate; rather it is oblique to the trench of the south American subduction zone. This direction may indicate a component of three-dimensional flow in the South American subduction system, consistent with inferences from elsewhere along the margin (e.g., Eakin et al., 2014; Long et al., 2016; Lynner & Beck, 2020).

6. Conclusion

We used the PS-SKS splitting technique to measure upper mantle anisotropy beneath the Pacific Ocean, a region in which splitting measurements using traditional *KS splitting techniques are hard to obtain due to a paucity of seismic stations. Our results indicate that seismic anisotropy is mostly caused by shear associated with the motion of the Pacific plate. A subtle rotation of upper mantle fast polarization directions north of Fiji may reflect three dimensional flow associated with the Vanuatu subduction zone.

Data Availability Statement

All USArray data (IRIS Transportable Array, 2003) are publicly available at IRIS (https://service.iris.edu/). The synthetic seismograms for this study were computed using AxiSEM3D which is publicly available at https://github.com/AxiSEMunity (Leng et al., 2016, 2019). SplitRacer_auto, a modified version of which was used in the splitting analysis, is available at https://www.geophysik.uni-frankfurt.de/64002762/Software (Link et al., 2022).

Acknowledgments
This work was funded by Yale University. We thank the Yale Center for Research Computing for providing the necessary research computing infrastructure for this study. The Generic Mapping Tools (Wessel & Smith, 1998) and ObsPy (Beyreuther et al., 2010) were used in this research. We thank Frederik Tilmann and an anonymous reviewer for constructive comments. We are grateful to the Yale seismology group for helpful discussions.

References

Barruol, G., Wüstefeld, A., & Bokelmann, G. (2009). *SKS-splitting-database*. Université de Montpellier, Laboratoire Géosciences. https://doi.org/10.18715/sks_splitting_database

Becker, T. W. (2012). On recent seismic tomography for the western United States. *Geochemistry, Geophysics, Geosystems*, *13*(1), Q01W10. https://doi.org/10.1029/2011GC003977

Becker, T. W., & Lebedev, S. (2021). Dynamics of the upper mantle in light of seismic anisotropy. In *Mantle convection and surface expressions* (pp. 257–282). American Geophysical Union (AGU). https://doi.org/10.1002/9781119528609.ch10

Beyreuther, M., Barsch, R., Krischer, L., Megies, T., Behr, Y., & Wassermann, J. (2010). Obspy: A python toolbox for seismology. *Seismological Research Letters*, *81*(3), 530–533. https://doi.org/10.1111/10.1785/gssrl.81.3.530

Chevrot, S. (2000). Multichannel analysis of shear wave splitting. *Journal of Geophysical Research*, *105*(B9), 21579–21590. https://doi.org/10.1029/2000JB900199

Coffin, M. F., Gahagan, L. M., & Lawver, L. A. (1997). *Present-day plate boundary digital data compilation*. Technical Report No. 174, (Vol. 199, pp. 1–6). University of Texas Institute for Geophysics. Retrieved from http://hdl.handle.net/2152/65603

Debayle, E., Dubuffet, F., & Durand, S. (2016). An automatically updated S-wave model of the upper mantle and the depth extent of azimuthal anisotropy. *Geophysical Research Letters*, *43*(2), 674–682. https://doi.org/10.1002/2015GL067329

DeMets, C., Gordon, R. G., & Argus, D. F. (2010). Geologically current plate motions. *Geophysical Journal International*, *181*(1), 1–80. https://doi.org/10.1111/j.1365-246X.2009.04491.x

Dziewonski, A. M., & Anderson, D. L. (1981). Preliminary reference Earth model. *Physics of the Earth and Planetary Interiors*, *25*(4), 297–356. https://doi.org/10.1016/0031-9201(81)90046-7

Eakin, C. M., Lithgow-Bertelloni, C., & Dávila, F. M. (2014). Influence of Peruvian flat-subduction dynamics on the evolution of western Amazonia. *Earth and Planetary Science Letters*, *404*, 250–260. https://doi.org/10.1016/j.epsl.2014.07.027

Eddy, C. L., Ekström, G., & Nettles, M. (2022). Three-dimensional seismic anisotropy in the Pacific upper mantle from inversion of a surface-wave dispersion data set. *Geophysical Journal International*, *231*(1), 355–383. https://doi.org/10.1093/gji/ggac194

Faccenda, M., & Capitanio, F. A. (2012). Development of mantle seismic anisotropy during subduction-induced 3-D flow. *Geophysical Research Letters*, *39*(11), L11305. https://doi.org/10.1029/2012GL051988

Fontaine, F. R., Barruol, G., Tommasi, A., & Bokelmann, G. H. R. (2007). Upper-mantle flow beneath French Polynesia from shear wave splitting. *Geophysical Journal International*, *170*(3), 1262–1288. https://doi.org/10.1111/j.1365-246X.2007.03475.x

Grund, M., & Ritter, J. R. (2018). Widespread seismic anisotropy in Earth's lowermost mantle beneath the Atlantic and Siberia. *Geology*, *47*(2), 123–126. https://doi.org/10.1130/G45514.1

Hicks, S. P., Nippress, S. E., & Rietbrock, A. (2012). Sub-slab mantle anisotropy beneath south-central Chile. *Earth and Planetary Science Letters*, *357–358*, 203–213. https://doi.org/10.1016/j.epsl.2012.09.017

IRIS Transportable Array. (2003). *USArray transportable array*. International Federation of Digital Seismograph Networks. https://doi.org/10.7914/SN/TA

Karato, S.-I. (2008). *Deformation of Earth materials: An introduction to the rheology of solid Earth*. Cambridge University Press. https://doi.org/10.1017/CBO9780511804892

Karato, S.-I., Jung, H., Katayama, I., & Skemer, P. (2008). Geodynamic significance of seismic anisotropy of the upper mantle: New insights from laboratory studies. *Annual Review of Earth and Planetary Sciences*, *36*(1), 59–95. https://doi.org/10.1146/annurev.earth.36.031207.124120

Kneller, E. A., van Keken, P. E., Karato, S.-I., & Park, J. (2005). B-type olivine fabric in the mantle wedge: Insights from high-resolution non-Newtonian subduction zone models. *Earth and Planetary Science Letters*, *237*(3–4), 781–797. https://doi.org/10.1016/j.epsl.2005.06.049

Lebedev, S., & Van Der Hilst, R. D. (2008). Global upper-mantle tomography with the automated multimode inversion of surface and S-wave forms. *Geophysical Journal International*, *173*(2), 505–518. https://doi.org/10.1111/j.1365-246X.2008.03721.x

Leng, K., Nissen-Meyer, T., & van Driel, M. (2016). Efficient global wave propagation adapted to 3-D structural complexity: A pseudospectral/spectral-element approach. *Geophysical Journal International*, *207*(3), 1700–1721. https://doi.org/10.1093/gji/ggw363

Leng, K., Nissen-Meyer, T., van Driel, M., Hosseini, K., & Al-Attar, D. (2019). AxiSEM3D: Broad-band seismic wavefields in 3-D global Earth models with undulating discontinuities. *Geophysical Journal International*, *217*(3), 2125–2146. https://doi.org/10.1093/gji/ggz092

Link, F., Reiss, M. C., & Rümpker, G. (2022). An automatized XKS-splitting procedure for large data sets: Extension package for SplitRacer and application to the USArray. *Computers & Geosciences*, *158*, 104961. https://doi.org/10.1016/j.cageo.2021.104961

Liu, K., Elsheikh, A., Lemnifi, A., Purevsuren, U., Ray, M., Refayee, H., et al. (2014). A uniform database of teleseismic shear wave splitting measurements for the western and central United States. *Geochemistry, Geophysics, Geosystems*, *15*(5), 2075–2085. https://doi.org/10.1002/2014GC005267

Long, M. D. (2013). Constraints on subduction geodynamics from seismic anisotropy. *Reviews of Geophysics*, *51*(1), 76–112. https://doi.org/10.1002/rog.20008

Long, M. D., & Becker, T. (2010). Mantle dynamics and seismic anisotropy. *Earth and Planetary Science Letters*, *297*(3–4), 341–354. https://doi.org/10.1016/j.epsl.2010.06.036

Long, M. D., Biryol, C. B., Eakin, C. M., Beck, S. L., Wagner, L. S., Zandt, G., et al. (2016). Overriding plate, mantle wedge, slab, and subslab contributions to seismic anisotropy beneath the northern Central Andean Plateau. *Geochemistry, Geophysics, Geosystems*, *17*(7), 2556–2575. https://doi.org/10.1002/2016GC006316

Lopes, E., Long, M. D., Karabinos, P., & Aragon, J. C. (2020). SKS splitting and upper mantle anisotropy beneath the southern New England Appalachians: Constraints from the dense SEISConn array. *Geochemistry, Geophysics, Geosystems*, *21*(12), e2020GC009401. https://doi.org/10.1029/2020GC009401

Lynner, C., & Beck, S. L. (2020). Subduction dynamics and structural controls on shear wave splitting along the South American convergent margin. *Journal of South American Earth Sciences*, *104*, 102824. https://doi.org/10.1016/j.jsames.2020.102824

Lynner, C., & Long, M. (2012). Evaluating contributions to SK(K)S splitting from lower mantle anisotropy: A case study from station DBIC, Cote D'Ivoire. *Bulletin of the Seismological Society of America*, *102*(3), 1030–1040. https://doi.org/10.1785/0120110255

Lynner, C., & Long, M. D. (2014). Lowermost mantle anisotropy and deformation along the boundary of the African LLSVP. *Geophysical Research Letters*, *41*(10), 3447–3454. https://doi.org/10.1002/2014GL059875

Niu, F., & Perez, A. M. (2004). Seismic anisotropy in the lower mantle: A comparison of waveform splitting of SKS and SKKS. *Geophysical Research Letters*, *31*(24), L24612. https://doi.org/10.1029/2004GL021196

Paczkowski, K., Montési, L. G. J., Long, M. D., & Thissen, C. J. (2014). Three-dimensional flow in the subslab mantle. *Geochemistry, Geophysics, Geosystems*, *15*(10), 3989–4008. https://doi.org/10.1002/2014GC005441

Panning, M. P., & Romanowicz, B. (2006). A three-dimensional radially anisotropic model of shear velocity in the whole mantle. *Geophysical Journal International*, *167*(1), 361–379. https://doi.org/10.1111/j.1365-246X.2006.03100.x

Panning, M. P., & Nolet, G. (2008). Surface wave tomography for azimuthal anisotropy in a strongly reduced parameter space. *Geophysical Journal International*, *174*(2), 629–648. https://doi.org/10.1111/j.1365-246X.2008.03833.x

Reiss, M., & Rümpker, G. (2017). SplitRacer: MATLAB code and GUI for semiautomated analysis and interpretation of teleseismic shear-wave splitting. *Seismological Research Letters*, *88*(2A), 392–409. https://doi.org/10.1785/0220160191

Russo, R., Gallego, A., Comte, D., Mocanu, V., Murdie, R., & VanDecar, J. (2010). Source-side shear wave splitting and upper mantle flow in the Chile Ridge subduction Region. *Geology*, *38*(8), 707–710. https://doi.org/10.1130/G30920.1

Savage, M. K. (1999). Seismic anisotropy and mantle deformation: What have we learned from shear wave splitting? *Reviews of Geophysics*, *37*(1), 65–106. https://doi.org/10.1016/10.1029/98RG02075

Silver, P. G. (1996). Seismic anisotropy beneath the continents: Probing the depths of geology. *Annual Review of Earth and Planetary Sciences*, *24*(1), 385–432. https://doi.org/10.1146/annurev.earth.24.1.385

Silver, P. G., & Chan, W. W. (1991). Shear wave splitting and subcontinental mantle deformation. *Journal of Geophysical Research*, *96*(B10), 16429–16454. https://doi.org/10.1029/91JB00899

Su, L., & Park, J. (1994). Anisotropy and the splitting of PS waves. *Physics of the Earth and Planetary Interiors*, *86*(4), 263–276. https://doi.org/10.1016/0031-9201(94)90125-2

Takeo, A., Kawakatsu, H., Isse, T., Nishida, K., Sugioka, H., Ito, A., et al. (2016). Seismic azimuthal anisotropy in the oceanic lithosphere and asthenosphere from broadband surface wave analysis of OBS array records at 60 Ma seafloor. *Journal of Geophysical Research: Solid Earth*, *121*(3), 1927–1947. https://doi.org/10.1002/2015JB012429

Tesoniero, A., Leng, K. D., Long, M., & Nissen-Meyer, T. (2020). Full wave sensitivity of SK(K)S phases to arbitrary anisotropy in the upper and lower mantle. *Geophysical Journal International*, *222*(1), 412–435. https://doi.org/10.1093/gji/ggaa171

Trabant, C., Hutko, A. R., Bahavar, M., Karstens, R., Ahern, T., & Aster, R. (2012). Data products at the IRIS DMC: Stepping stones for research and other applications. *Seismological Research Letters*, *83*(5), 846–854. https://doi.org/10.1785/0220120032

Walpole, J., Wookey, J., Masters, G., & Kendall, J. M. (2014). A uniformly processed data set of SKS shear wave splitting measurements: A global investigation of upper mantle anisotropy beneath seismic stations. *Geochemistry, Geophysics, Geosystems*, *15*(5), 1991–2010. https://doi.org/10.1002/2014GC005278

Walsh, E., Arnold, R., & Savage, M. K. (2013). Silver and Chan revisited. *Journal of Geophysical Research: Solid Earth*, *118*(10), 5500–5515. https://doi.org/10.1002/jgrb.50386

Wessel, P., & Smith, W. H. F. (1998). New, improved version of generic mapping tools released. *Eos, Transactions American Geophysical Union*, *79*(47), 579. https://doi.org/10.1029/98EO00426

Wolf, J., Creasy, N., Pisconti, A., Long, M. D., & Thomas, C. (2019). An investigation of seismic anisotropy in the lowermost mantle beneath Iceland. *Geophysical Journal International*, *219*(Supplement_1), S152–S166. https://doi.org/10.1093/gji/ggz312

Wolf, J., & Long, M. D. (2022). Slab-driven flow at the base of the mantle beneath the northeastern pacific ocean. *Earth and Planetary Science Letters*, *594*, 117758. https://doi.org/10.1016/j.epsl.2022.117758

Wolf, J., & Long, M. D. (2023). Lowermost mantle structure beneath the central Pacific Ocean: Ultralow velocity zones and seismic anisotropy. *Geochemistry, Geophysics, Geosystems*, *24*(6), e2022GC010853. https://doi.org/10.1029/2022GC010853

Wolf, J., Long, M. D., Creasy, N., & Garnero, E. (2023). On the measurement of Sdiff splitting caused by lowermost mantle anisotropy. *Geophysical Journal International*, *233*(2), 900–921. https://doi.org/10.1093/gji/ggac490

Wolf, J., Long, M. D., Leng, K., & Nissen-Meyer, T. (2022a). Constraining deep mantle anisotropy with shear wave splitting measurements: Challenges and new measurement strategies. *Geophysical Journal International*, *230*(1), 507–527. https://doi.org/10.1093/gji/ggac055

Wolf, J., Long, M. D., Leng, K., & Nissen-Meyer, T. (2022b). Sensitivity of SK(K)S and ScS phases to heterogeneous anisotropy in the lowermost mantle from global wavefield simulations. *Geophysical Journal International*, *228*(1), 366–386. https://doi.org/10.1093/gji/ggab347

Yu, Y., & Park, J. (1993). Upper mantle anisotropy and coupled-mode long-period surface waves. *Geophysical Journal International*, *114*(3), 473–489. https://doi.org/10.1111/j.1365-246X.1993.tb06981.x

Yuan, K., & Beghein, C. (2014). Three-dimensional variations in Love and Rayleigh wave azimuthal anisotropy for the upper 800 km of the mantle. *Journal of Geophysical Research: Solid Earth*, *119*(4), 3232–3255. https://doi.org/10.1002/2013JB010853

Zhu, H., Yang, J., & Li, X. (2020). Azimuthal anisotropy of the North American upper mantle based on full waveform inversion. *Journal of Geophysical Research: Solid Earth*, *125*(2), e2019JB018432. https://doi.org/10.1029/2019JB018432